International Journal of Heat and Mass Transfer 52 (2009) 5130–5140

Contents lists available at ScienceDirect

International Journal of Heat and Mass Transfer

journal homepage: www.elsevier.com/locate/ijhmt

Numerical study of convective flow with condensation of a pure fluid in capillary regime

M. Miscevic *, P. Lavieille, B. Piaud

Université de Toulouse, 118 Route de Narbonne, UMR n5213 LAPLACE, Bâtiment 3R1b3, 31062 Toulouse cedex 09, France

ARTICLE INFO

Article history:
Received 9 March 2009
Received in revised form 13 May 2009
Accepted 13 May 2009
Available online 13 June 2009

Keywords:
Condensation
Microchannel
Model
Capillary regime
Heat transfer

ABSTRACT

A stationary 2-phase flow model with condensation in the capillary regime, based on a separate flow approach was developed. One of the specificities of the model is that it takes into account the coupling between a cylindrical interface (region with a thin film of liquid) and a hemispherical interface (main meniscus at the end of the condensation region). A specific algorithm was developed for numerical resolution to overcome the difficulty related to the presence of a free boundary condition. Analysis of the liquid–vapour interface profiles and the various local parameters allowed us to establish the heat and mass transfer laws for the particular type of regime studied. We analysed the dominant effects of this type of flow, which are characterised by dimensionless numbers *Ca* (capillary number) and *Bo* (boiling number), representing the competition between the capillary, viscous and phase-change effects. The effects due to the difference in density between the two phases and to the Reynolds number were also studied. We show that the mean heat transfer coefficients are driven by the profile of the interface. Hence, in certain situations, even when the liquid film becomes thinner on average an unexpected lowering of the efficiency of heat transfer is obtained. These effects are closely related to the coupling between the thin liquid film region and the main meniscus.

1. Introduction

Unlike evaporation and boiling, condensation in micro-channels has been the object of relatively few studies. Most have been carried out with the aim of optimising condensers for air-conditioning systems [1–14] where the mass flow rates in the channel are from a hundred to several hundred kg m^{-2} s^{-1}. To model flow and heat transfer in these conditions, most authors have used correlative approaches. In early work, the approaches consisted in attempting to adapt laws established for condensers with a conventional diameter (i.e. of the order of 1 cm) to condensation flows in micro-channels. To give just one example, Shin and Kim [15] compared the pressure drops obtained experimentally during R134a condensation flow in a 0.691 mm diameter channel with the results of Friedel's correlation [16], which was developed for tubes of larger diameters. A good agreement was found only for values of mass flow greater than 400 kg m^{-2} s^{-1}. For such mass flows, the main factors affecting phase structures and pressure drop are inertia and interfacial and wall friction. It is therefore not surprising to obtain similar behaviour since in both cases, capillary and gravitational phenomena are weak compared to inertia and friction.

It is therefore for the smallest mass fluxes that the effects of miniaturisation are felt most strongly. The study of Médéric et al. [17] revealed flow regimes visualised directly in horizontal channels of 10, 1.1 and 0.56 mm. The range of mass fluxes is limited to values of under 20 kg m^{-2} s^{-1}, which corresponds to values typical of applications involving 2-phase cooling loops with capillary pumping (LHP – Loop Heat Pipe or CPL – Capillary Pumped Loop). With such low working fluid flows, the roles of gravity and capillarity become crucial.

Wu and Cheng [11] observed droplet nucleation in the entrance region of the channel. Downstream of this zone, the droplets formed a continuous film at the periphery of the tube. This annular structure is terminated by a hemispherical meniscus, downstream of which bubbles become periodically detached.

For a fluid with a higher wettability, neither Begg et al. [2] nor Médéric et al. [18,19] observed a droplet nucleation zone on the wall. The detachment of bubbles downstream of the capillary zone (annular zone + hemispherical meniscus zone) was reported by Médéric et al. for mass fluxes over a critical value of about 7 kg m^{-2} s^{-1} when the working fluid was *n*-pentane in a tube with an internal diameter of 0.56 mm. The mechanisms at the origin of bubble detachment reported in refs [18,19] are the destabilisation of the interface formed by the extended meniscus under the joint effects of capillarity, interfacial friction and phase change.

---

* Corresponding author. Tel.: +33 561558307; fax: +33 561556021.
E-mail addresses: marc.miscevic@laplace.univ-tlse.fr (M. Miscevic), pascal.lavieille@laplace.univ-tlse.fr (P. Lavieille), benjamin.piaud@laplace.univ-tlse.fr (B. Piaud).

0017-9310/$ - see front matter © 2009 Elsevier Ltd. All rights reserved.
doi:10.1016/j.ijheatmasstransfer.2009.05.004

Nomenclature

Bo	boiling number
Ca	capillary number
e	wall thickness (m)
G	mass flux (kg m^{-2} s^{-1})
h	heat transfer coefficient (internal when no subscript) (W m^{-2} K^{-1})
H	global heat transfer coefficient (W m^{-2} K^{-1})
L	length of the condensation zone (m)
ℓ_v	latent heat of vaporisation (J kg^{-1})
$\dot{m}$	mass flow rate (kg s^{-1})
Nu	Nusselt number
p	pressure (Pa)
R	radial position of the interface (m)
R_1, R_2	main curvature radii (m)
Re	Reynolds number
R_t	internal radius of the channel (m)
T	temperature (K)
U	velocity (m s^{-1})
x	quality

Greek symbols

ϵ	small arbitrary value (m)
Γ	volumic rate of phase change (kg m^{-3} s^{-1})
δ	liquid film thickness (m)
λ	thermal conductivity (W m^{-1} K^{-1})
μ	dynamic viscosity (Pa s)
ν	kinematic viscosity (m^2 s^{-1})
ξ	constant $(= \overline{U^2}/\overline{U}^2)$
ρ	density (kg m^{-3})
σ	surface tension (N m^{-1})
τ	shear stress (N m^{-2})

Superscripts

-	reduced value
$*$	dimensionless value

Subscripts

c	connection between main meniscus and liquid film zones
i	interface
ℓ	liquid
lim	limit: at the extremity of the stream
m	mean
out	external
sat	saturation
v	vapour
w	wall

The analysis of this type of instability in a stream of condensing vapour firstly requires a good understanding of the stable capillary regime. This type of regime is of particular interest for CPLs operating in microgravity or for miniature set-ups [20].

The aim of the present paper is to propose a model of the condensation flow in the capillary regime and an associated numerical resolution method. Such study is complementary of available models in literature for film condensation observed at higher flow rates [21,22]. Local analysis of the individual roles of the different mechanisms involved in structuring the liquid and vapour phases will improve the understanding of the processes necessary for scaling and optimising this type of heat exchanger.

The structure of the paper is as follows: the model, based on a description of the flow with separate flow approach is presented in Section 2; in Section 3, the algorithm for the numerical resolution of the model is detailed. Particular stress is placed on the method used to solve the problem of the free boundary condition. Finally, analyses of the results in terms of flow and heat transfer are presented in Section 4 as a function of the dimensionless parameters used to characterise the elementary mechanisms involved.

2. Physical and mathematical models

2.1. Geometric configuration

In this section, we propose a stationary model for the condensation of a stream of vapour in a narrow-bore channel. The geometric configuration considered and the boundary conditions imposed are those used in the experimental study of Médéric et al. [18,19] and are schematised in Fig. 1. The channel, composed of a wall of thickness e, has a circular cross-section with an internal radius of R_t. Conductive heat transfers through the wall (of thermal conductivity λ_w) are assumed to be purely radial, corresponding to the commonest situation, where the wall is thermally thin. The channel is cooled by a fluid at temperature T_{out}, which remains constant all along the channel, with a convective heat transfer coefficient h_{out} between the outer wall and the coolant that also remains uniform and constant.

A mass flow of saturated vapour is fixed at the entrance to the channel. Upon contact with the cool wall of the channel, the vapour condenses and a film of liquid forms. Its thickness varies with the quality, which is itself dependent on the axial position. The film of liquid ends in an almost hemispherical meniscus when the quality tends towards zero. Its position is one of the unknowns in the problem. The cooling of the liquid downstream of the end of the meniscus is not dealt with in this paper.

Experimentally, this type of flow structure is found in low mass flux configurations in a microgravity environment or in miniaturised set-ups. In both cases, gravity does not intervene and the flow can be taken to be axisymetric.

2.2. Mathematical model in stationary regime

The modelling approach developed here describes the liquid and vapour phases separately. In each of the phases, the parameters are the average over a cross-section, but attention was paid to respecting continuity conditions at the interface.

The continuity equations for the liquid and vapour phases can be written, respectively, as:

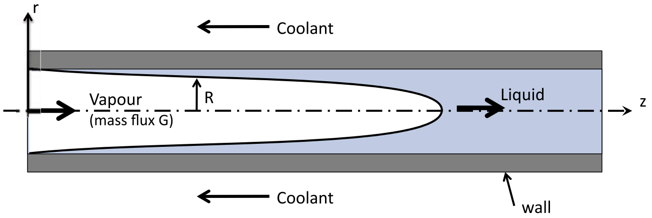

Fig. 1. Geometrical configuration studied and the imposed boundary conditions. Cooling is from a water jacket at constant temperature and with a constant heat transfer coefficient over the whole length of the channel. Flow is assumed to be axisymmetric.

$$\frac{d\left(\rho_\ell\left(1-\frac{R^2}{R_t^2}\right)U_\ell\right)}{dz}=-\Gamma \tag{1}$$

$$\frac{d\left(\rho_v\frac{R^2}{R_t^2}U_v\right)}{dz}=\Gamma \tag{2}$$

where Γ represents the volumic rate of phase change. By convention its sign is negative for condensation.

The equations for the conservation of momentum in each of the phases are written:

$$\frac{d\left(\xi_\ell\rho_\ell\left(1-\frac{R^2}{R_t^2}\right)U_\ell^2\right)}{dz}=-\left(1-\frac{R^2}{R_t^2}\right)\frac{dp_\ell}{dz}-\tau_{w\ell}\frac{2}{R_t}+\tau_i\frac{2R}{R_t^2} \tag{3}$$

$$\frac{d\left(\xi_v\rho_v\frac{R^2}{R_t^2}U_\ell^2\right)}{dz}=-\frac{R^2}{R_t^2}\frac{dp_v}{dz}-\tau_i\frac{2R}{R_t^2} \tag{4}$$

The ratio R^2/R_t^2 represents the void fraction, defined here by the ratio between the area occupied by the vapour phase and the total cross-section area. The coefficients ξ_ℓ and ξ_v represent the ratio between the mean of the square of the velocity and the square of the mean velocity in a cross-section, for the liquid and vapour phases, respectively. Assuming that the velocity profile corresponds to that of Couette flow in the liquid phase and Poiseuille flow in the vapour phase, these coefficients are equal to 4/3.

From the enthalpy balance, ignoring the sensible heat, we can determine the volumic rate of phase change Γ:

$$\Gamma=G\frac{dx}{dz}=-\frac{2H(T_{sat}-T_{out})}{R_t\ell_v} \tag{5}$$

where H represents the overall heat transfer coefficient between the working fluid and the coolant. Considering the exchange to be purely radial and transfers purely conductive in liquid films, it can be expressed as:

$$H=\frac{1}{\frac{R_t}{h_{out}(R_t+e)}+\frac{R_t}{\lambda_w}\ln\left(\frac{R_t+e}{R_t}\right)+\frac{R_t}{\lambda_\ell}\ln\left(\frac{R_t}{R}\right)} \tag{6}$$

The radial only heat transfer assumption was widely used with success for such micro devices (e.g. [21,22]). Indeed, in the liquid phase, the temperature evolves weakly according to the axial position.

Closure of the system is obtained by writing the Laplace–Young equation as:

$$p_v-p_\ell=\sigma\left(\frac{1}{R\sqrt{1+\left(\frac{dR}{dz}\right)^2}}-\frac{\frac{d^2R}{dz^2}}{\left(1+\left(\frac{dR}{dz}\right)^2\right)^{3/2}}\right) \tag{7}$$

Balance Eqs. (1)–(5) and the Laplace–Young equation (7) make up the system of equations to be resolved. In order to facilitate numerical resolution, the equations are rearranged to give the following system:

$$\frac{dU_\ell}{dz}=\frac{2H(T_{sat}-T_{out})R_t}{\rho_\ell\left(R_t^2-R^2\right)\ell_v}+\frac{2U_\ell R}{R_t^2-R^2}\frac{dR}{dz} \tag{8}$$

$$\frac{dU_v}{dz}=-\frac{2H(T_{sat}-T_{out})R_t}{\rho_v R^2\ell_v}-\frac{2U_v}{R}\frac{dR}{dz} \tag{9}$$

$$\frac{dp_\ell}{dz}=-\frac{2\tau_w R_t}{R_t^2-R^2}+\frac{2\tau_i R}{R_t^2-R^2}-\frac{8}{3}\rho_\ell U_\ell\frac{dU_\ell}{dz}+\frac{8}{3}\rho_\ell U_\ell^2\frac{R}{R_t^2-R^2}\frac{dR}{dz} \tag{10}$$

$$\frac{dp_v}{dz}=-\frac{2\tau_i}{R}-\frac{8}{3}\rho_v U_v\frac{dU_v}{dz}-\frac{8}{3}\frac{\rho_v U_v^2}{R}\frac{dR}{dz} \tag{11}$$

$$\frac{d^2R}{dz^2}=\left(1+\left(\frac{dR}{dz}\right)^2\right)^{3/2}\left(\frac{1}{\sigma}(p_\ell-p_v)+\frac{1}{R\sqrt{1+\left(\frac{dR}{dz}\right)^2}}\right) \tag{12}$$

in which the unknowns are: $U_\ell(z),\ U_v(z),\ p_\ell(z),\ p_v(z)$ and $R(z)$.

As detailed below in Section 2.4, the length L of the stream of vapour must be added to the list of unknowns to take into account the fact that the problem to be resolved has a free boundary condition. Hence, an additional equation must be considered; it can be obtained by noting that in stationary regime, the mass flow rate of the vapour phase is nil at longitudinal position $z=L$:

$$\dot{m}_{v(z=L)}=0 \tag{13}$$

Before this system of equations can be resolved, the friction laws at the wall and at the interface must be defined, as must the limit conditions.

2.3. Friction laws

The wall shear stress is defined assuming Couette flow in the liquid. This gives:

$$\tau_w=\frac{16}{Re_\ell}\frac{1}{2}\rho_\ell U_\ell^2 \tag{14}$$

Re_ℓ is the Reynolds number of the liquid flow considering the hydraulic diameter as the characteristic dimension:

$$Re_\ell=\frac{\rho_\ell U_\ell}{\mu_\ell}\left(2\frac{R_t^2-R^2}{R_t}\right) \tag{15}$$

As the liquid velocity profile is considered to be linear, the velocity at the interface is therefore equal to $2U_\ell$, where U_ℓ is the mean velocity of the liquid in a cross-section. The interfacial shear stress is estimated from Wallis' equation [23]:

$$\tau_i=\frac{16}{Re_v}\frac{1}{2}\rho_v(U_v-2U_\ell)^2\left[1+75\left(1-\left(\frac{R}{R_t}\right)^2\right)\right] \tag{16}$$

with

$$Re_v=\frac{\rho_v(U_v-2U_\ell)2R}{\mu_v} \tag{17}$$

Although this equation was established for water–air flow, it was successfully used by Médéric [24] in the present configuration.

2.4. Boundary conditions

The imposed boundary conditions were chosen as close as possible to the experimental conditions of previous studies [18,19].

At the pipe inlet, the flow arrives with an imposed mass flux G in the form of saturated vapour. We therefore have:

$$R_{(z=0)}=R_t \tag{18}$$

$$U_{v(z=0)}=\frac{G}{\rho_v} \tag{19}$$

A convective heat transfer coefficient $h_{out}=c^{te}$ is imposed between the outer wall of the tube and the coolant, which has a constant temperature of T_{out}. In the following, h_{out} is set to different values: a small value leads to uniform heat flux although a very high value corresponds to uniform wall temperature.

In the experimental study, the pressure of the liquid (n-pentane) is roughly equal to the pressure at the pipe outlet (i.e. atmospheric pressure in the experimental set-up). As the flow of the liquid is not dealt with in the present paper, the pressure at the outlet will be set at the end of the stream of vapour, i.e. at $z=L$ which corresponds to the end of the condensation zone:

$$p_{\ell(z=L)}=p_o \tag{20}$$

Note that in the examples studied here, the variations of pressure are very low compared to the mean pressure. The saturation temperature of the fluid is therefore assumed to remain constant.

For configurations where the pressure drop is greater or when the average pressure is lower, the dependence of T_{sat} on pressure must be taken into account using the Clapeyron equation.

Downstream of the condensation zone, the condition of symmetry implies that:

$$R_{(z=L)} = 0 \tag{21}$$

As condensation is complete, the flow condition in the steady state at this same position means that:

$$U_{\ell(z=L)} = \frac{G}{\rho_\ell} \tag{22}$$

The 5 boundary conditions (18)–(22) and the set of Eqs. (8)–(13) compose the mathematical model of flow in a capillary regime with a vapour–liquid change of phase. Its resolution is not trivial since one of the limit positions remains to be found, the value of L being one of the unknowns of the problem. The problem is therefore one with a free boundary condition requiring the use of a particular algorithm for resolution.

3. Resolution algorithm

As presented so far, the mathematical model is difficult to resolve numerically: the longitudinal position of one of the boundary is unknown.

This quite particular situation explains why Eq. (13) is dealt with as an equation belonging to the model rather than as a boundary condition.

The algorithm is designed on the basis of a finite difference schema. In order to make the schema explicit, it is assumed that all the variables at one of the extremities of the vapour stream are known. To do so, the values of the unknown variables at that extremity are arbitrarily fixed. The system of discretised equations is thus easily resolved in an explicit manner. A dichotomy is then applied to the initial arbitrary values in order to satisfy the conditions at the other extremity of the stream.

We chose to fix the values of the variables at the downstream extremity of the vapour stream ($z = L$), where 4 boundary conditions have already been imposed (see Section 2.4).

For this longitudinal position, the value of $\frac{dR}{dz}$ remains to be set in order to have a second boundary condition for the Laplace–Young equation (7), and the value of p_v for the equation of conservation of momentum (4).

Rather than fixing both these values arbitrarily, the variables p_v and $\frac{dR}{dz}$ are expressed as a function of parameter R_{lim} which represents the radius of curvature of the main meniscus at the extremity of the stream which is perfectly spherical at this location owing to its axial symmetry. In addition, in order to obtain a finite value for $\frac{dR}{dz}$, the conditions at this boundary are set at $z = (L - \epsilon)$, where ϵ has a very small arbitrary value (it is checked later that the solution is independent of ϵ) (Fig. 2). In order to calculate the two main curvatures, the planes perpendicular to the interface and including the normal to the surface were defined as follows. The plane used to describe what is known as the second curvature is the plane containing the axis of symmetry and the normal. The first curvature is therefore the curvature of the surface that is observed in the plane perpendicular to the previous one but also contains the normal to the surface (Fig. 2).

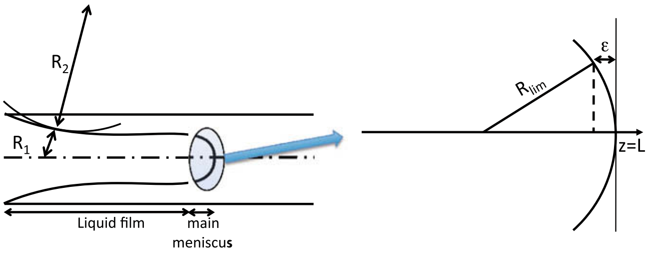

Fig. 2. Diagram of the shift in value ϵ of the position where we fix the boundary conditions of the stream of vapour and definition of the two radii of curvature of the interface: R_1 and R_2.

For these two boundary conditions, we therefore obtain:

$$\left(\frac{dR}{dz}\right)_{z=L-\epsilon} = -\frac{R_{lim} - \epsilon}{\sqrt{R_{lim}^2 - (R_{lim} - \epsilon)^2}} \tag{23}$$

$$p_{v(z=L-\epsilon)} = p_{\ell(z=L-\epsilon)} + \frac{2\sigma}{R_{lim}} \tag{24}$$

the 4 other boundary conditions at $z = L - \epsilon$ being:

$$R_{(z=L-\epsilon)} = \sqrt{R_{lim}^2 - (R_{lim} - \epsilon)^2} \tag{25}$$

$$U_{v(z=L-\epsilon)} = \frac{2HR_t\epsilon(T_{sat} - T_{out})}{\rho_v \ell_v \left(R_{lim}^2 - (R_{lim} - \epsilon)^2\right)} \tag{26}$$

$$U_{\ell(z=L-\epsilon)} = \frac{G\ell_v R_t^2 - 2HR_t\epsilon(T_{sat} - T_{out})}{\rho_\ell \ell_v \left(R_t^2 - \left(R_{lim}^2 - (R_{lim} - \epsilon)^2\right)\right)} \tag{27}$$

$$p_{\ell(z=L-\epsilon)} = p_o \tag{28}$$

The boundary conditions are set by fixing an initial value for ϵ and R_{lim}. The system of equations is then resolved by starting at position $z = L - \epsilon$ and moving against the flow using a 4th order Runge–Kutta method with Matlab® software.

Two situations can then occur:

- either the resolution of the system provides a location where the thickness of the liquid film tends to zero but not the liquid flow rate: in this event the value of R_{lim} is decreased and the system is re-resolved.
- or, in contrast, the flow of liquid is nil but the thickness of the film is not. Here, value of R_{lim} is increased.

A dichotomy on R_{lim} leads to convergence towards the solution which simultaneously satisfies the two constraints at the upstream extremity of the stream of vapour (i.e. zero liquid film thickness and flow) corresponding to conditions (18) and (19).

4. Results and analyses

4.1. Dimensionless numbers

By making the lengths dimensionless using R_t, velocities of liquid and vapour using $\frac{G}{\rho_\ell}$ et $\frac{G}{\rho_v}$, respectively, and the pressures using $\frac{2\sigma}{R_t}$, it is easily shown that Eqs. (8)–(12) become the following dimensionless expressions (where an asterisk denotes dimensionless magnitudes):

$$\frac{1 - R^{*2}}{2}\frac{dU_\ell^*}{dz^*} = Bo + U_\ell^* R^* \frac{dR^*}{dz^*} \tag{29}$$

$$\frac{R^{*2}}{2}\frac{dU_v^*}{dz^*} = -Bo - U_v^* R^* \frac{dR^*}{dz^*} \tag{30}$$

$$\begin{aligned}\frac{1}{Ca}\frac{dp_\ell^*}{dz^*} = {} & -4\frac{U_\ell^*}{\left(1 - R^{*2}\right)^2} + 4\left[\frac{1}{1 - R^{*2}} + 75\right]\left(\overline{\nu}U_v^* - 2\overline{\mu}U_\ell^*\right) \\ & - \frac{2}{3}Re_{\ell 0}\left(U_\ell^* \frac{dU_\ell^*}{dz^*} - \frac{R^*}{1 - R^{*2}} U_\ell^{*2} \frac{dR^*}{dz^*}\right)\end{aligned} \tag{31}$$

$$\frac{1}{Ca}\frac{dp_v^*}{dz^*} = -4\frac{1+75(1-R^{*2})}{R^{*2}}\left(\overline{\nu}U_v^* - 2\overline{\mu}U_\ell^*\right) - \frac{2}{3}\frac{Re_{\ell 0}}{\overline{\rho}}\left(U_v^*\frac{dU_v^*}{dz^*} + \frac{U_v^{*2}}{R^*}\frac{dR^*}{dz^*}\right) \tag{32}$$

$$\frac{d^2R^*}{dz^{*2}} = \left[1+\left(\frac{dR^*}{dz^*}\right)^2\right]^{3/2}\left[2\left(p_\ell^* - p_v^*\right) + \frac{1}{R^*\sqrt{1+\left(\frac{dR^*}{dz^*}\right)^2}}\right] \tag{33}$$

Groups of dimensionless numbers appear: the capillary number, the boiling number, the reduced dynamic viscosity, the reduced density and the Reynolds number of the liquid when flowing in single-phase:

$$Ca = \frac{\mu_\ell G}{\rho_\ell \sigma} \tag{34}$$

$$Bo = \frac{H(T_{sat} - T_{out})}{G\ell_v} \tag{35}$$

$$\overline{\mu} = \frac{\mu_v}{\mu_\ell} \tag{36}$$

$$\overline{\rho} = \frac{\rho_v}{\rho_\ell} \tag{37}$$

$$Re_{\ell 0} = \frac{2GR_t}{\mu_\ell} \tag{38}$$

The reduced kinematic viscosity $\overline{\nu} = \frac{\nu_v}{\nu_\ell}$ is calculated from $\overline{\nu} = \frac{\overline{\mu}}{\overline{\rho}}$.

These dimensionless numbers are then considered below to represent the evolution of different variables. It can be noted that $\overline{\mu}$ varies over a very limited range considering the fluids most often used. Its influence will therefore not be investigated in the present paper.

The numerical resolution of the system of equations enables the radial position R of the liquid–vapour interface to be determined as a function of the longitudinal position z. The values of Ca, Bo, $\overline{\mu}$, $\overline{\rho}$ and $Re_{\ell 0}$ are fixed independently at desired values, by adjusting the values of σ, $(T_{sat} - T_{out})$, μ_v, ρ_v and G. The values of the other thermophysical and geometric parameters are arbitrarily imposed at the values presented in the study of Médéric et al. [18,19].

4.2. Profile of the interface and local analyses

Two examples of calculated interface profiles are presented in Fig. 3 and correspond to two values of vapour stream length ($Bo = 0.04$ and 0.2). The values of the other dimensionless numbers are $Ca = 10^{-5}$, $\overline{\mu} = 3\cdot 10^{-2}$, $\overline{\rho} = 5\cdot 10^{-3}$ and $Re_{\ell 0} = 10$. Fig. 3a presents these profiles versus the longitudinal position z^*. The meniscus extends over a much greater distance for $Bo = 0.04$. A small value of the boiling number corresponds to a low mean density of heat flux. As the mass fluxes, and thus the power to be extracted to obtain complete condensation, are identical in the two cases presented then the lower Bo, the larger the area of heat exchange required.

In addition to its influence on the length of the meniscus, the boiling number plays a role on the shape of the meniscus. Making the axial position dimensionless by means of the length L, a deformation of the interface is clearly seen to appear (Fig. 3b and c) for

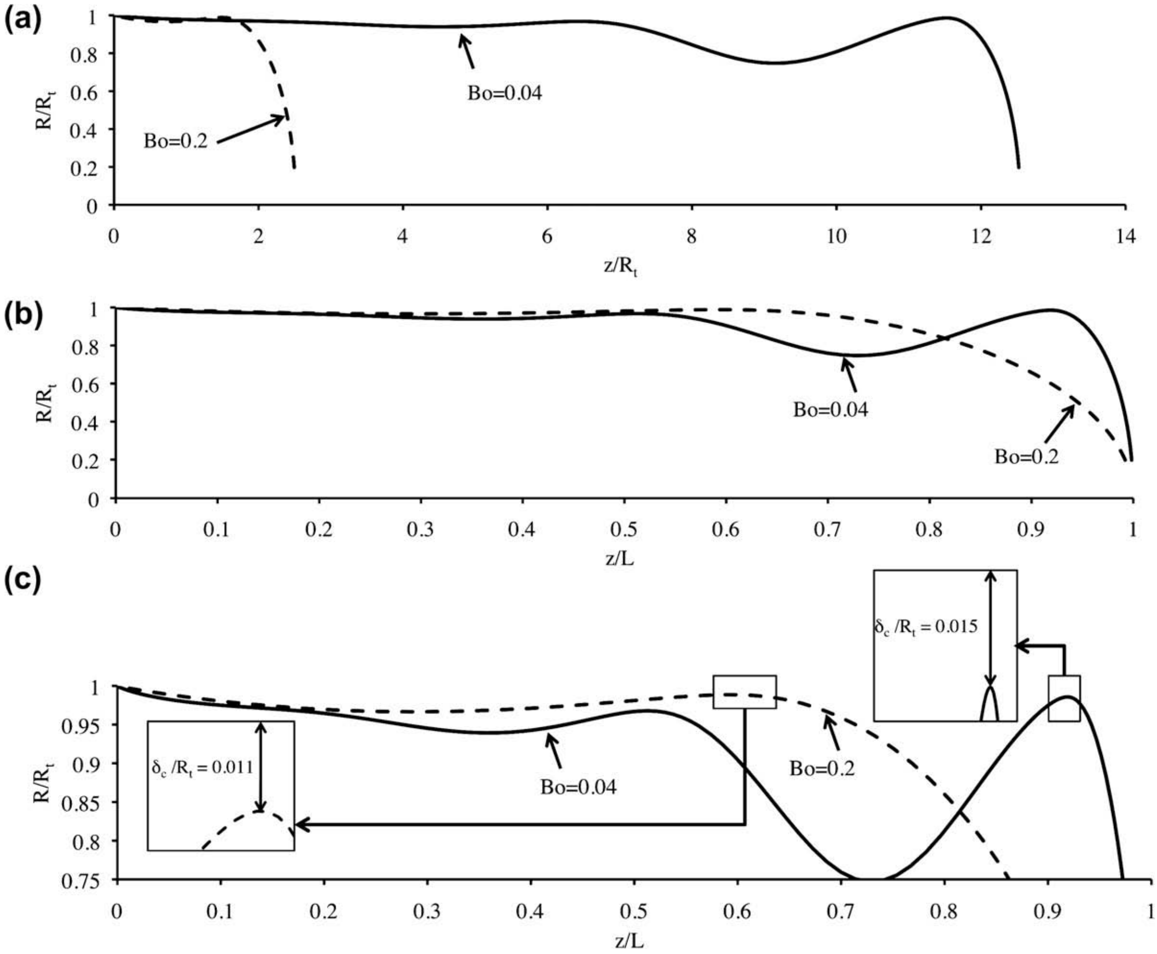

Fig. 3. Examples of profiles calculated for the liquid–vapour interface for boiling numbers $Bo = 0.04$ and $Bo = 0.2$ ($Ca = 10^{-5}$, $\overline{\mu} = 3\cdot 10^{-2}$, $\overline{\rho} = 5\cdot 10^{-3}$ and $Re_{\ell 0} = 10$); (a) as a function of z/R_t; (b) of the reduced position z/L; and (c) Zoom of figure b close to the wall.

$Bo = 0.04$. In the area of the thin film of liquid, the loss of pressure due to viscous friction (interface and wall) is low (a few Pa, see Fig. 4). The average curvature at position z in this zone is more or less identical to the curvature observed in the plane perpendicular to the axis of the micro-tube. The thickness of the film of liquid increases progressively owing to condensation.

In the junction region between the thin film of liquid and the main meniscus (cf. Fig. 2, $z \approx L - R_t$), the influence of the second radius of curvature becomes preponderant. Indeed, this second curvature, which had a value of close to zero in the previous section (the interface that can be observed is almost cylindrical), on going downstream becomes approximately equal to $1/R_t$ (the interface takes the shape of a hemispherical cap of radius approaching R_t). As the vapour pressure hardly varies over this very short distance, the multiplication of the average curvature by about 2 leads to a sharp increase in the pressure gradient in the liquid, which must be compensated by viscous friction. Consequently, in this transition zone, the increase in viscous friction is obtained through a strong decrease in the liquid film thickness (reaching a minimum δ_c, Fig. 3c) leading to a strong increase in the mass flux of the liquid (Fig. 5).

The variations of the second curvature of the interface are less strong when the value of Bo is high owing to the small length of the meniscus. Indeed, for such values of Bo, the length over which the second radius of curvature has a significant effect on the value of the mean curvature represents a large proportion of the length of the 2-phase zone. This is illustrated in Fig. 6, which represents the variation of the maximum thickness of the film of liquid in the thin-film region (i.e. without considering the main meniscus zone) plotted against the boiling number. It can be observed that for high values of Bo, the maximum thickness only represents a few percent of the radius of the tube, illustrating the low interface deformation. As the value of Bo decreases, and hence the length L increases, the thickness δ_{max} increases rapidly until it represents more than 50% of the radius of the tube. For values of Bo lower than 0.02, no stationary solution is obtained. The absence of a stationary solution is not in conflict with the experimental results of Médéric et al. [19] who show that beyond a critical flow rate threshold, non-stationary phenomena appear. In these conditions, a non-stationary model must be developed to analyse the stability of this type of flow.

4.3. Laws of heat transfer

The applications that can be concerned by the present study involve heat exchangers working in microgravity or miniaturised exchangers in which the mass flux is low. For the scaling of this type of component, it is useful to know the laws governing the variation of the average heat transfer coefficients. The local coefficient concerning internal heat exchange at position z is defined as:

$$h(z) = \frac{\lambda_\ell}{R_t \ln\left(\frac{R_t}{R}\right)} \tag{39}$$

From this, we can deduce the mean internal Nusselt number considering the channel diameter as the characteristic dimension:

$$Nu_m = \frac{h_m 2R_t}{\lambda_\ell} = \frac{1}{L}\int_0^L \frac{-2}{\ln\left(1 - \frac{\delta(z)}{R_t}\right)} dz \tag{40}$$

where $\delta(z)$ is the local thickness of the liquid film ($\delta(z) = R_t - R(z)$).

4.3.1. Influence of heat flux

As previously indicated in the hypotheses of the mathematical model, the value of the mean internal Nusselt number is solely dependent on the thickness profile of the liquid film, i.e. the shape of the interface. The shape in turn depends on the boundary conditions imposed on the channel wall. When the external heat transfer coefficient is low compared to the internal one, it is the outside that limits the transfers and thus the situation is one of uniform heat flux. In contrast, if the external heat transfer coefficient is very high, the wall will have a uniform temperature equal to that of the coolant (the conductive resistance of the wall then being fixed at 0).

The variations of the mean internal Nusselt number as a function of the boiling number are reported in Fig. 7 for the two situations (uniform heat flux and constant wall temperature).

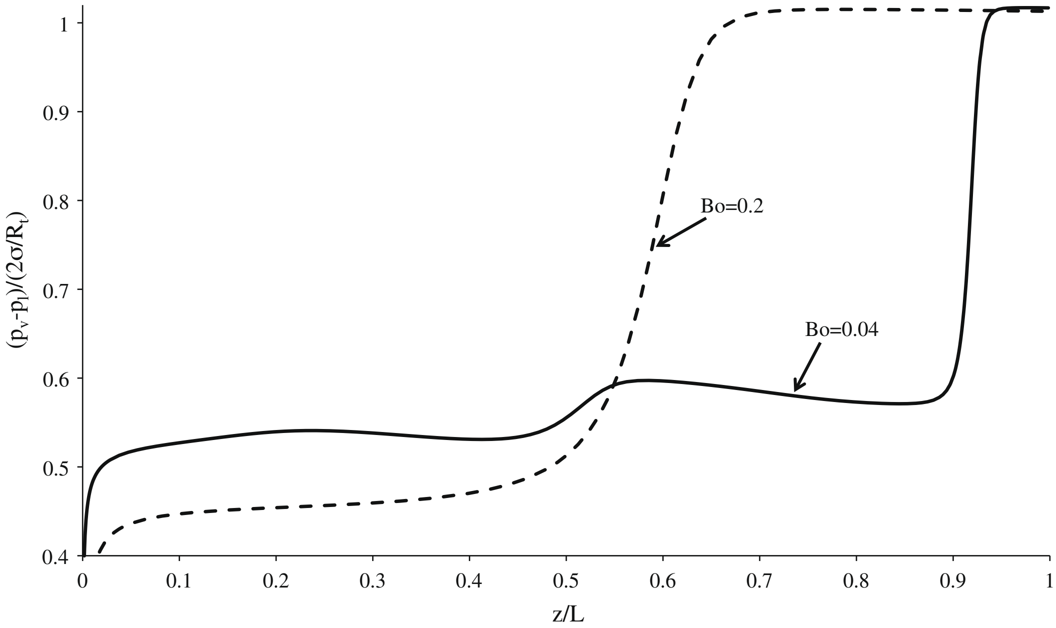

Fig. 4. Examples of profiles of dimensionless capillary pressure for boiling numbers $Bo = 0.04$ and $Bo = 0.2$ ($Ca = 10^{-5}$, $\overline{\mu} = 3 \cdot 10^{-2}$, $\overline{\rho} = 5 \cdot 10^{-3}$ and $Re_{\ell 0} = 10$). In the two configurations, the obtained variations are mainly due to those in the liquid phase, the pressure of the vapour remaining nearly constant.

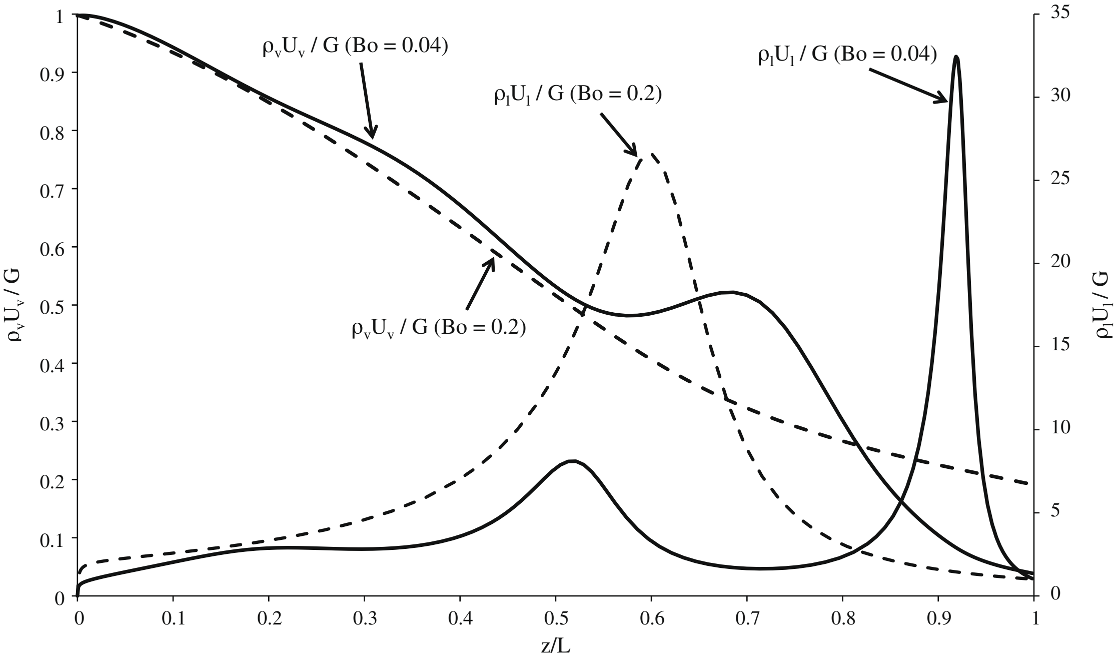

Fig. 5. Examples of the non-dimensional mass flux versus the reduced position for $Bo = 0.04$ and $Bo = 0.2$ ($Ca = 10^{-5}$, $\overline{\mu} = 3 \cdot 10^{-2}$, $\overline{\rho} = 5 \cdot 10^{-3}$ and $Re_{\ell 0} = 10$). The values correspond to the interface profiles given in Fig. 3.

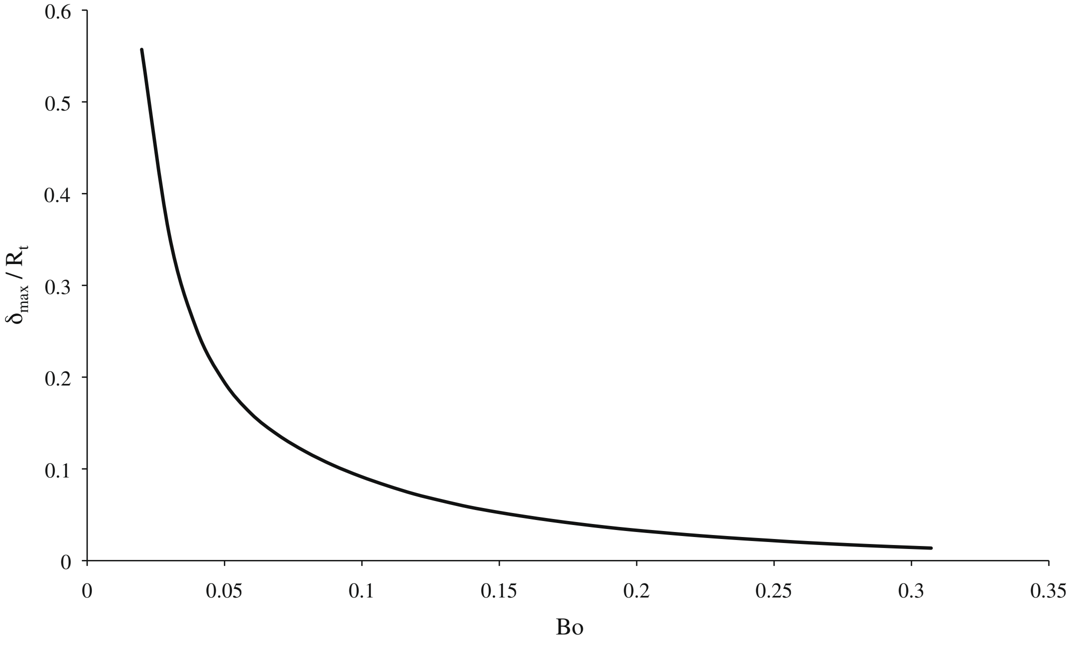

Fig. 6. Maximum dimensionless thickness of the liquid film versus the boiling number ($Ca = 10^{-5}$, $\overline{\mu} = 3 \cdot 10^{-2}$, $\overline{\rho} = 5 \cdot 10^{-3}$ and $Re_{\ell 0} = 10$).

Note that the boiling number, which is by definition linked to the change of phase, is calculated from H_m by the expression:

$$Bo = \frac{H_m(T_{sat} - T_{out})}{G\ell_v} \tag{41}$$

where H_m is the mean global heat transfer coefficient such that $H_m 2\pi R_t L \Delta T$ represents the total heat flux:

$$H_m = \frac{1}{L}\int_0^L \left(\frac{1}{h_{out}}\frac{R_t}{R_t + e} + \frac{1}{h(z)} + \frac{R_t}{\lambda_w \ln\left(\frac{R_t + e}{R_t}\right)}\right)^{-1} dz \tag{42}$$

Numerical calculations are performed considering values of the boiling number down to 0.02, which correspond to a maximum length of the meniscus of about 25 times the radius of the channel. The calculations for $Bo > 0.3$ lead to lengths of the order of 1.5 the channel radius.

In this range of values of Bo, the mean internal Nusselt number varies from 30 to 80 when the wall temperature is constant and 40–100 when the heat flux is uniform. The increase obtained is not intuitive since it implies that drawing out the meniscus does not give more intense transfers.

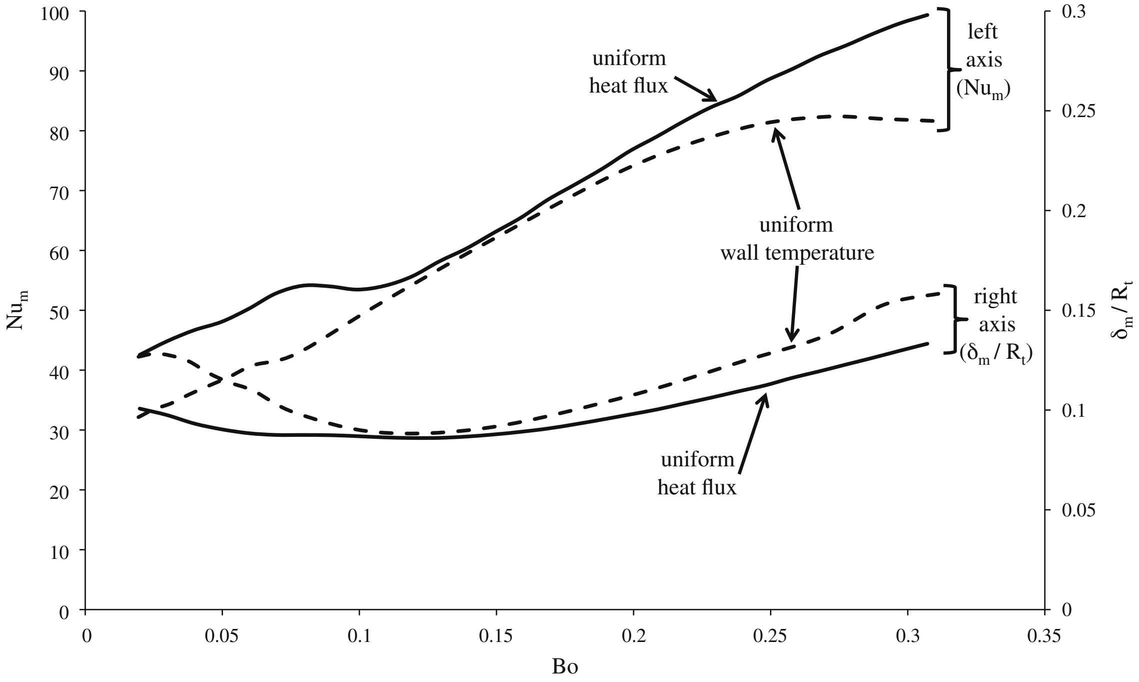

Fig. 7. Mean internal Nusselt number and mean liquid film thickness versus the boiling number ($Ca = 10^{-5}$, $\overline{\mu} = 3 \cdot 10^{-2}$, $\overline{\rho} = 5 \cdot 10^{-3}$ and $Re_{\ell 0} = 10$): solid lines show the case of uniform heat flux, dotted lines show the case of uniform wall temperature.

To study this behaviour, we plotted the variations of film thickness versus the boiling number (Fig. 7). It can be seen that the shorter the meniscus, the greater the mean thickness of the liquid film. Nu_m and δ_m are both increasing functions of *Bo*. It therefore appears that increasing the mean thickness of the liquid film, unexpectedly leads to an increase in heat transfer. This behaviour is due to the shape change of the interface as *Bo* varies. Indeed, the shorter the meniscus, the lower the values of δ_{max} and δ_c, which implies that the film becomes thinner in the thin-film region (Fig. 6). At the same time, the mean thickness of the film increases (Fig. 7). This antagonism in the variations of (δ_{max}, δ_c) and of δ_m is related to the relative weight of the main meniscus region in the calculation of the mean thickness of the liquid film. We therefore have:

- a zone of thin film where the heat transfers are more intense,
- a main meniscus region whose length (divided by *L*) is increased and where transfers are almost invariable (and much lower than the transfers occurring in the thin film).

In terms of intensification of heat transfer, the positive effect obtained in the thin film region is greater than the negative effect arising from the increased role of the main meniscus. The overall result is a rise in the mean Nusselt number in spite of the increase in δ_m.

4.3.2. Influence of capillary-viscous effects

The intensity of heat transfer therefore depends on the distribution of the liquid and vapour phases in the channel. In addition to the imposed heat flux (that can be pictured by the boiling number), this distribution depends on the value of the capillary number. To illustrate this dependence, we plotted the variation of the mean Nusselt number against *Bo* for various values of *Ca*, and the modifications of the interface profile caused by the variation of the value of *Ca* for $Bo = 0.15$ (Figs. 8 and 9, respectively).

The results in Fig. 8 show that Nu_m increases with *Bo*, whatever the value of *Ca*. However, for a fixed value of *Bo*, an increase on *Ca* caused a clear decrease in Nu_m. For a low value of the capillary number, the surface tension effects are high and the concavity of the interface changes little (Fig. 9 curve $Ca = 10^{-7}$). By increasing the value of *Ca*, the effects of surface tension decrease; the interface presents a more sharply curved profile (Fig. 9 curve $Ca = 5 \cdot 10^{-5}$), leading to a reduction in global heat transfer over the whole length of the meniscus.

A conclusion similar to that drawn in the previous section can therefore be proposed: the variations in the curvature of the liquid–vapour interface profile (i.e. the numerous changes of sign in the second curvature) has the consequence that it decreases the values of the average heat transfer coefficients, whether this deformation is induced by the decrease in the heat flux at the wall or by the decrease of the capillary effects compared to the viscous effects.

Fig. 8 also shows that at low values of $Ca (Ca \lesssim 5 \cdot 10^{-6})$, the tendency in the variation of Nu_m changes sharply for values of *Bo* lower than about 0.08, i.e. when *L* becomes about 6 or 7 times higher than R_t. This critical length is close to $2\pi R_t$ which corresponds to the shortest unstable wavelength of the Rayleigh–Plateau capillary instability. To conclude as to the possibility of the existence of these stationary solutions, a non-stationary approach, which includes the effects of confinement and of phase change must be developed, as must an analysis of the associated stability.

4.3.3. Influence of the density contrast

A third dimensionless number that affects the distribution of the phases is the ratio $\overline{\rho}$ of the densities of the vapour and liquid phases. A value of $5 \cdot 10^{-3}$ for $\overline{\rho}$ is high and corresponds to the order of magnitude of the ratio for *n*-pentane. For water, the value of $\overline{\rho}$ is one order of magnitude lower.

A three-dimensional representation (Fig. 10) of the general appearance of the liquid–vapour interface is given for $\overline{\rho} = 5 \cdot 10^{-4}$ and $\overline{\rho} = 5 \cdot 10^{-3}$, the other parameters are identical in both cases. There is a distinctive modification of the interface shape. At $\overline{\rho} = 5 \cdot 10^{-3}$, the amplitude of the deformation of the liquid films is clearly much greater than for $\overline{\rho} = 5 \cdot 10^{-4}$. This density ratio appears in the 2nd and 1st terms on the right sides of Eqs. (31) and (32), respectively. An increase in $\overline{\rho}$ leads to an increase in the effect of

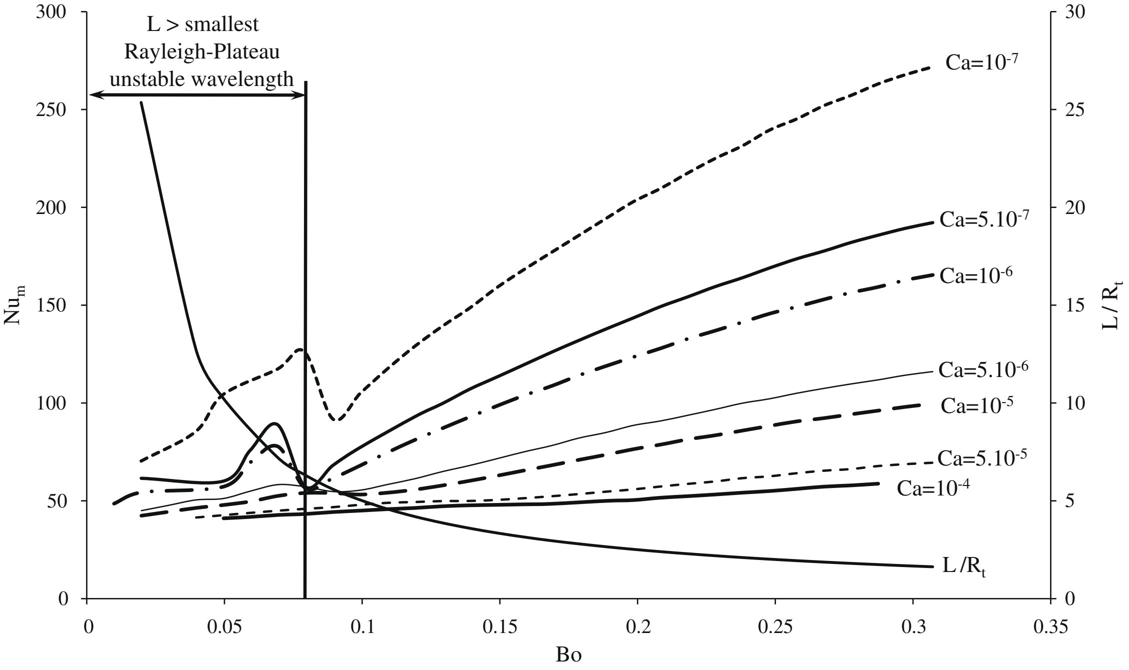

Fig. 8. Mean internal Nusselt number versus the boiling number for different capillary numbers ($\overline{\mu} = 3 \cdot 10^{-2}$, $\overline{\rho} = 5 \cdot 10^{-3}$ and $Re_{\ell 0} = 10$) with uniform heat flux boundary condition.

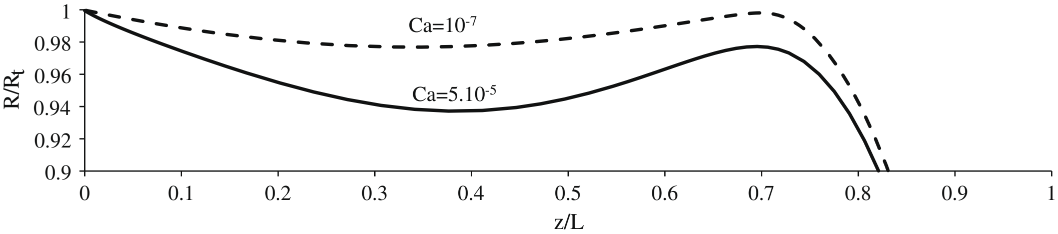

Fig. 9. Interface profiles ($Bo = 0.15$, $\overline{\mu} = 3 \cdot 10^{-2}$, $\overline{\rho} = 5 \cdot 10^{-3}$ and $Re_{\ell 0} = 10$) for two capillary numbers and with uniform heat flux boundary condition.

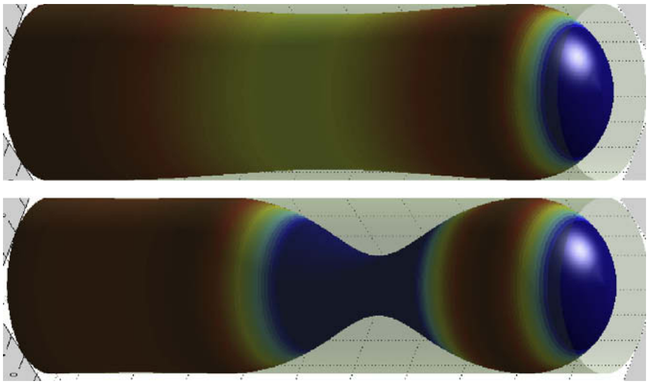

Fig. 10. Illustration of the effect of a tenfold increase in $\overline{\rho}$ on the deformation of the interface profile when the capillary number is low ($Ca = 10^{-7}$): the upper figure was obtained for $\overline{\rho} = 5 \cdot 10^{-4}$ and the lower figure for $\overline{\rho} = 5 \cdot 10^{-3}$. In both cases the meniscus length was $L = 7.2R_t$.

these 2 terms, i.e. a reduction in viscous friction. The shape of the interface is then mainly determined by the capillary effects (remember that, in this example, *Ca* is very small), which explains the large deformation obtained. Indeed, when the meniscus is sufficiently drawn out, the deformation is determined by the radius of curvature R_1. As discussed previously, non-stationary modelling would probably lead to the appearance of a capillary instability of the Rayleigh–Plateau type. It can however, be noted that the influence of $\overline{\rho}$ becomes rapidly attenuated as the capillary number is increased.

4.3.4. Discussion about the low Reynolds hypothesis

Most microfluidics studies assume the low Reynolds hypothesis. In the case of condensation flow, making this assumption means that the liquid and vapour phase accelerations are ignored, as are the effects of phase changes in the equations of conservation of momentum (31) and (32). In this section, we propose to determine the point at which the low Reynolds hypothesis becomes no-longer relevant. So, let us consider an intermediate boiling number ($Bo = 0.144$) and different values of the capillary number. The results in terms of mean Nusselt number and mean dimensionless thicknesses are reported in Fig. 11. Similar behaviour can be seen irrespective of *Ca* for low $Re_{\ell 0}$ numbers. In this case, we can indeed see an indifference of Nu_m with respect to the Reynolds number. This justifies the standard low Reynolds hypothesis. However, the results show that beyond $Re_{\ell 0} \approx 100$, noticeable effects can be seen on the variation of Nu_m. Moreover, these effects differ as the capillary number changes: for low values of *Ca*, an increase in $Re_{\ell 0}$ intensifies transfer, while the opposite is noted at higher values of *Ca*.

An interpretation of this difference of behaviour can be made from the observation of the interface profiles obtained for different values of *Ca* and $Re_{\ell 0}$ (Fig. 12). When the capillary number is low

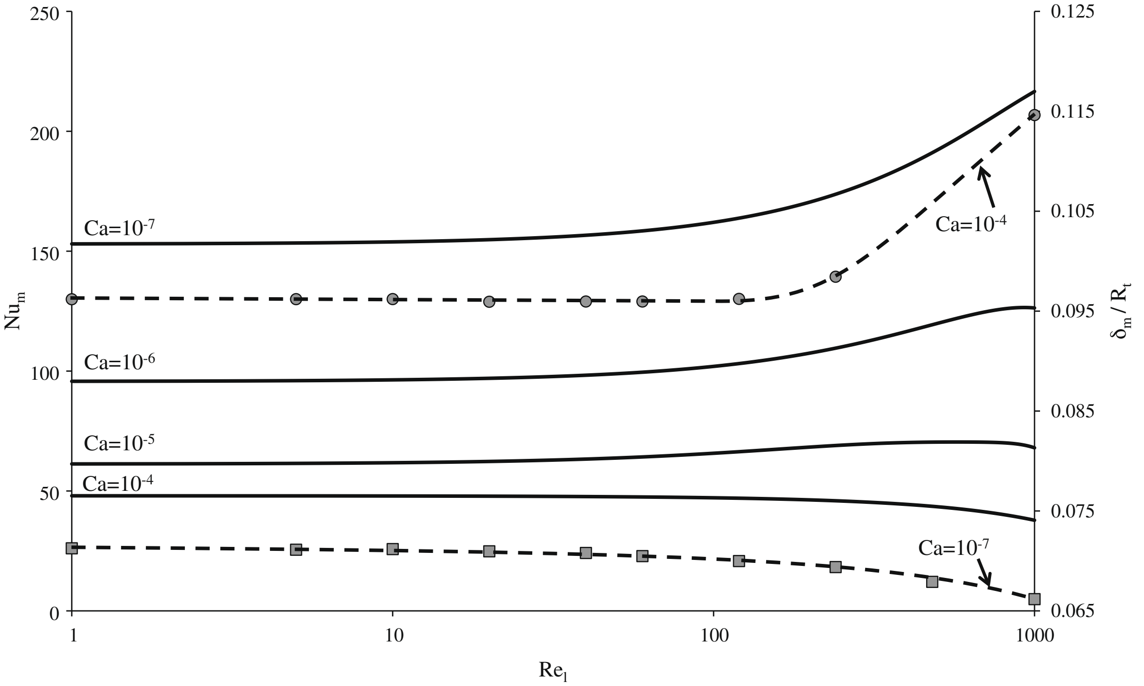

Fig. 11. Internal Nusselt number (solid lines) and mean dimensionless thickness (dotted lines) versus the liquid Reynolds number for different capillary numbers ($Bo = 0.144,\ \overline{\rho} = 5 \cdot 10^{-3}$).

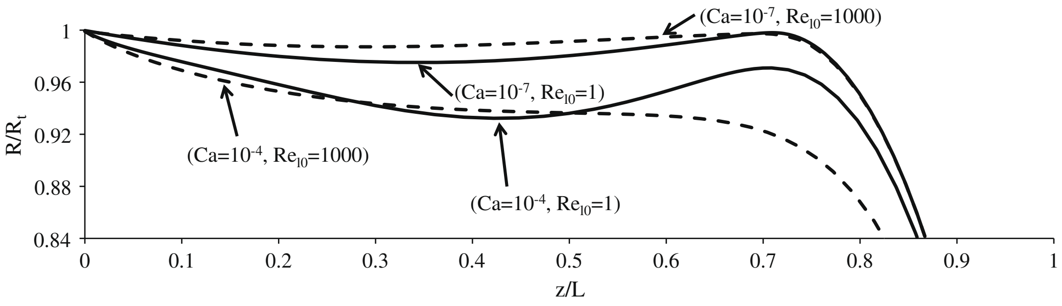

Fig. 12. Interface profiles for various values of the capillary number and the Reynolds number with uniform heat flux boundary condition ($Bo = 0.144,\ \overline{\mu} = 3 \cdot 10^{-2},\ \overline{\rho} = 5 \cdot 10^{-3}$).

($Ca = 10^{-7}$) and as the Reynolds number is raised from 1 to 1000 the profile of the interface becomes less irregular. This smoothing causes a reduction in the mean thickness of the film of liquid (Fig. 11) and an increase of Nu_m.

For higher values of the capillary number (10^{-4} in this example), an increase in the Reynolds number also leads to smoothing of the interface. However, a high value of Ca does not allow a thin film of liquid to be maintained in the transition region between the main meniscus and the thin film (δ_c, see Fig. 3). Indeed, as mentioned in paragraph 4.2, in this transition region the sharp capillary pressure jump caused by the variation of the mean curvature leads to local thinning of the liquid film. The higher the capillary number, the less intense the thinning. Thus, a high value of Ca with a high value of $Re_{\ell 0}$ leads to thicker liquid film and consequently reduced heat transfer.

5. Conclusions

Condensation in the capillary regime can be modelled by separately considering the two phases in the model. We established a system of equations based on this approach and proposed a resolution algorithm that enables a numerical solution to be found for this type of problem with a free boundary condition.

The results were analysed taking 4 dimensionless numbers into account: the boiling number, the capillary number, the density ratio of the phases and the liquid Reynolds number.

The general shape of the interfaces obtained over the range of values studied for the dimensionless numbers includes a region with a thin layer of liquid and a main meniscus region with a hemispherical end. Analysing the flow revealed that the pressure drop due to friction in the liquid mainly occurs at the junction between these two regions. The pressure drop is caused by the thinning of the liquid film which increases as Ca decreases. This influences the shape of the interface and thus affects heat transfer.

From a heat transfer point of view, it has been shown that (mean) thinning of the liquid film can reduce efficiency owing to the change in the spatial distribution of the phases. Hence, when the interface is deformed under the effect of a decrease in the boiling number or an increase in the capillary number, the average Nusselt number decreases. If strongly amplified, this deformation is likely to destabilise the interface and form liquid bridges, leading to a transition in the flow regime.

Acknowledgements

Financial supports from GIP ANR (ANR-06-BLAN-0119-01) and from PR Energie/CNRS (MICROCOND) are gratefully acknowledged.

References

[1] M.K. Dobson, J.C. Chato, Condensation in smooth horizontal tubes, ASME J. Heat Transfer 120 (1998) 213–393.

[2] E. Begg, D. Khrustalev, A. Faghri, Complete condensation of forced convection two-phase flow in a miniature tube, ASME J. Heat Transfer 121 (1999) 904–915.

[3] A. Cavallini, G. Censi, D. Del Col, L. Doretti, G.A. Longo, L. Rosetto, Experimental investigation on condensation heat transfer and pressure drop of new HFC refrigerants (R134a, R125, R32, R410A, R236ea) in a horizontal smooth tube, Int. J. Refrig. 24 (2001) 73–87.

[4] A. Tabatabai, A. Faghri, A new two-phase flow map and transition boundary accounting for surface tension effects in horizontal miniature and micro tubes, ASME J. Heat Transfer 123 (2001) 958–968.

[5] W.-W.W. Wang, T.D. Radcliff, R.T. Christensen, A condensation heat transfer correlation for millimeter-scale tubing with flow regime transition, Exp. Thermal Fluid Sci. 26 (2002) 473–485.

[6] J.R. Baird, D.F. Fletcher, B.S. Haynes, Local condensation heat transfer rates in fine passages, Int. J. Heat Mass Transfer 46 (2003) 4453–4466.

[7] A. Cavallini, G. Censi, D. Del Col, L. Doretti, G.A. Longo, L. Rosetto, C. Zilio, Condensation inside and outside smooth and enhanced tubes – a review of recent research, Int. J. Refrig. 26 (2003) 373–392.

[8] J. El Hajal, J.R. Thome, A. Cavallini, Condensation in horizontal tubes. Part 1: two-phase flow pattern map, Int. J. Heat Mass Transfer 46 (2003) 3349–3363.

[9] J.R. Thome, J. El Hajal, A. Cavallini, Condensation in horizontal tubes. Part 2: new heat transfer model based on flow regimes, Int. J. Heat Mass Transfer 46 (2003) 3365–3387.

[10] Y. Chen, P. Cheng, Condensation of steam in silicon microchannels, Int. Commun. Heat Mass Transfer 32 (2005) 175–183.

[11] H.Y. Wu, P. Cheng, Condensation flow patterns in silicon microchannels, Int. J. Heat Mass Transfer 48 (2005) 2186–2197.

[12] J.R. Thome, Update on advances in flow pattern based two-phase heat transfer models, Exp. Thermal Fluid Sci. 29 (3) (2005) 341–349.

[13] A. Cavallini, D. Del Col, L. Doretti, M. Matkovic, L. Rossetto, C. Zilio, Two-phase frictional pressure gradient of R236ea, R134a and R410A inside multi-port mini-channels, Exp. Thermal Fluid Sci. 29 (7) (2005) 861–870.

[14] T.M. Bandhauer, A. Agarwal, S. Garimella, Measurement and modeling of condensation heat transfer coefficients in circular microchannels, ASME J. Heat Transfer 128 (10) (2006) 1050–1059.

[15] J.S. Shin, M.K. Kim, An experimental study of condensation heat transfer inside a mini-channel with a new measurement technique, Int. J. Multiphase Flow 30 (2004) 311–325.

[16] L. Friedel, Improved pressure drop correlation for horizontal and vertical two-phase pipe flow, in: European Two-phase Flow Group Meeting, Ispra, Italy, 1976, paper n2.

[17] B. Médéric, M. Miscevic, V. Platel, P. Lavieille, J.L. Joly, Experimental study of flow characteristics during condensation in narrow channels: influence of diameter channel on structure patterns, Superlatt. Microstruct. 35 (2004) 573–586.

[18] B. Médéric, P. Lavieille, M. Miscevic, Void fraction invariance property of complete condensation flow inside a capillary glass tube, Int. J. Multiphase Flow 31 (9) (2005) 1049–1056.

[19] B. Médéric, P. Lavieille, M. Miscevic, Heat transfer analysis according to condensation flow structures in a minichannel, Exp. Thermal Fluid Sci. 30 (2006) 785–793.

[20] M. Miscevic, B. Médéric, P. Lavieille, U. Soupremanien, V. Serin, Condensation in capillary-driven two-phase loops, Microgravity Sci. Technol. 19 (3-4) (2007) 116–120.

[21] H.S. Wang, J.W. Rose, Film condensation in horizontal circular-section microchannels, in: 5th International Symposium on Multiphase Flow, Heat Mass Transfer and Energy Conversion, Xi'an, China, 2005.

[22] H.S. Wang, J.W. Rose, Film condensation in horizontal microchannels: effect of channel shape, Int. J. Thermal Sci. 45 (2006) 1205–1212.

[23] G.B. Wallis, One-dimensional Two-phase Flow, McGraw-Hill, Inc., 1969.

[24] B. Médéric, Etude de la condensation convective en mini-tube: analyse des instabilités, Ph.D. thesis, Université Paul Sabatier, Toulouse, France, 2004.